Control System Design and Thrust Analysis of an Unmanned Surface Cleaning Vessel With a Novel Pump-Valve Propulsion System

YAOJING LUO, JIAOYAN AI, JIANWU ZHENG, AND JUFENG WANG

College of Electrical Engineering, Guangxi University, Nanning 530000, China

Corresponding author: Jiaoyan Ai (shinin@vip.163.com)

ABSTRACT This article presents a specialized control system for an unmanned surface cleaning vessel (USCV) employing a pump-valve propulsion system. The system has three operational modes, including manual remote-control mode, self-automated cruise mode, and self-locking remote-control mode. In the manual remote-control mode, users remotely control the vessel by means of a motion-control joystick. In the self-automated cruise mode, the control system is capable of detecting obstacles and automatically controlling the pump-valve propulsion system in response to feedback signals from sensors. The self-locking remote-control mode functions similarly to the first mode, except that the joystick controls the vessel motion in accordance with a single established joystick-actuation pattern. The control system is supported by a commercially available remote controller with wireless communication technology. The functionality of the combined control and pump-valve propulsion system is verified by computational fluid dynamics simulations and experimental tests conducted using a prototype USCV. The combined control and pump-valve propulsion system is demonstrated to be a cost-effective, simple, and innovative platform that is suitable for use with USCVs.

INDEX TERMS USCV, pump-valve propulsion, operational modes, CFD, motion states.

NOMENCLATURE
PROPULSION SYSTEM PARAMETERS
1A	Left side rear outlet
1B	Right side rear outlet
2A	Left side rear normally closed magnetic valve
2B	Right side rear normally closed magnetic valve
3A	Left side fore normally closed magnetic valve
3B	Right side fore normally closed magnetic valve
4A	Left side fore outlet
4B	Right side fore outlet
5A	Left side normally opened magnetic valve
5B	Right side normally opened magnetic valve
6A	Left side submerged pump
6B	Right side submerged pump
7A	Left side middle fore outlet
7B	Right side middle fore outlet
8A	Left side water flow inlet
8B	Right side water flow inlet

CONTROL PARAMETERS
K_p	Duty cycle control function
M	Multiplication factor
F_c	Correction function
θ	Pump power control term
D	Change rate factor
α	Pump power compensation factor
P_{max}	Maximum pump output power (W)
U_p	Pump drive voltage (V)
I_p	Pump current (A)
P_{act}	Actual pump power (W)
$\partial_{U(3\times3)}$	Generalized thrust vector
(X_U, Y_U)	Thrust force vector
N_U	Yaw moment of force (N)
M_U	Total mass of vessel (kg)
$I_{(3\times3)}$	Three-dimensional unit matrix
I_Z	Rotary inertia

$O_{(3\times3)}$	Three-dimensional null matrix
ω_U	Angular vessel velocity (rad/s)
V_U	Linear vessel velocity (dm/s)
F_{1A}	Counter-thrust of 1A (N)
F_{1B}	Counter-thrust of 1B (N)
F_{4A}	Counter-thrust of 4A (N)
F_{4B}	Counter-thrusts of 4B (N)
F_M	Joint forces of 7A and 7B (N)
F_U	Resultant vessel thrust (N)
X_U	Thrust along the X-axis direction (N)
Y_U	Thrust along the Y-axis direction (N)
G	Gravity point
T_{out}	Outlet thrust (N)
ε	Fluid density (g/cm^3)
Q	Flow rate of a given propulsion outlet (L/s)
V_{in}	Flow velocity of inlets 8A and 8B (dm/s)
V_{out}	Flow velocity of a given outlet (dm/s)
T_{loss}	Thrust losses (N)
T_{in}	Inlet thrust (N)
T_{out}	Outlet thrust (N)
η_T	Thrust efficiency

ACRONYMS

USCV	Unmanned surface cleaning vessel
USV	Unmanned surface vessel
TVCS	Thrust vector control system
USART	Universal synchronous/asynchronous receiver/transmitter
USB	Universal serial bus
CFD	Computational fluid dynamics
ESC	Electronic speed controller
GPIO	General-purpose input/output
SPI	Serial peripheral interface
TTL	Transistor-transistor logic
LED	Light-emitting diode
DC	Direct current
NMOS	N-channel metal oxide semiconductor
PWM	Pulse-width modulation
DTU	Data transfer unit

I. INTRODUCTION

Floating object collection is routinely employed to preserve the natural marine environment, and two main approaches are generally adopted for this purpose, which include manual and automatic collection [1]–[5]. Automatic collection operations have been increasingly applied in recent years, and have commonly adopted unmanned surface cleaning vessels (USCVs) in a wide variety of freshwater and marine settings. A number of USCVs have been developed for this purpose based on embedded control systems [6]–[9]. However, most

of these vessel control systems are complex and expensive, which greatly detracts from their wide-scale use due to a lack professional knowledge and money. Moreover, the blades of conventional propellers employed on unmanned surface vessels (USVs) can become entangled with floating objects such as plastic bottles and fishing lines [10]–[12]. Furthermore, the blades of conventional USV propellers can do harm to aquatic organisms.

The above-discussed deficiencies in past USCV developments has generated considerable interest in developing more reliable, efficient, and ecologically-friendly marine propulsion technologies, and, in particular, water jet control systems. For example, a vectored water jet propulsion method was proposed in 2013 for autonomous USVs [13]. Here, the reaction thrust of the water jet produced by a volumetric water pump was directionally controlled using a vectored nozzle. Improved maneuverability for underwater vehicles was provided in 2018 by the development of a high-pressure water jet propulsion system combined with a thrust vector control system (TVCS) [14]. Recently, a novel spherical underwater robot with a hybrid propulsion system, including vectored water-jet and propeller thrusters, was proposed [15]. Hybrid propulsion systems not only can increase the hydrodynamic thrust of underwater robots in restricted spaces, but decrease the noise level by switching from propeller operation to water-jet propulsion. Finally, we have developed a pump-valve propulsion system and a dedicated control system that can operate stably in a wide variety of freshwater and marine environments [16]. These past studies have demonstrated the vital role of propulsion systems in controlling the movement of USVs.

The present study addresses the above-discussed issues by presenting a specialized control system for a USCV employing a pump-valve propulsion system using a commercially available AT10 remote controller combined with an ARM-based microprocessor. The proposed design represents an improvement over our past work [16]. The system has three operational modes, including manual remote-control mode, self-automated cruise mode, and self-locking remote-control mode. In the manual remote-control mode, users remotely control the vessel by means of a motion-control joystick. In the self-automated cruise mode, the control system is capable of detecting obstacles and automatically controlling the propulsion system in response to feedback signals from sensors. The self-locking remote-control mode functions similarly to the first mode, except that the joystick controls the vessel motion in accordance with a single established joystick-actuation pattern. The present work is an extension of USV propulsion technology [17]–[19]. Wireless maneuvering control functions, such forward and backward motion or turning in place, are realized through a universal synchronous/asynchronous receiver/transmitter (USART) and a universal serial bus (USB) cable [20], where the control system downloads target files to a custom-made master board to facilitate maneuvering control [21], [22]. The controller program designed to manipulate the USCV
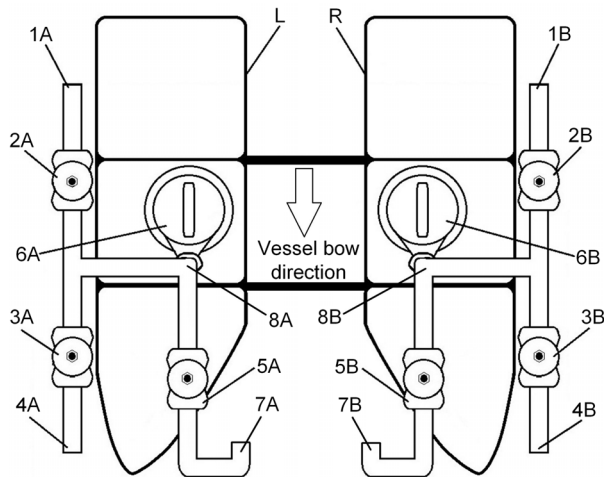
FIGURE 1. Schematic illustrating the USCV design scheme employing the proposed pump-valve propulsion system (top view).

remotely according to the three operational modes offers the beneficial features of high-speed response and reliable wireless communication [23]–[25]. The propulsion system achieves articulated USCV motion by employing two submerged pumps as water jet generators [26], with six magnetic valves as the jet controllers. Both water jets are generally employed simultaneously because their individual thrust efficiency is less than that of propellers. The functionality of the combined control and pump-valve propulsion system is verified by computational fluid dynamics (CFD) simulations and experimental tests conducted using a prototype USCV. The proposed USCV is thereby demonstrated to operate steadily without malfunction under a variety of conditions. Accordingly, the combined control and pump-valve propulsion system is demonstrated to represent a cost-effective, simple, and innovative platform that is suitable for use with USCVs. The proposed control and pump-valve propulsion system is applicable to a wide variety of watercraft, including underwater robots [27], [28], USVs, and even military vessels.

The remainder of this report is organized as follows. The basic operational principles of the pump-valve propulsion system are presented in Section II. The system architecture is presented in Section III. The overall structure of the system software is presented in Section IV. Section V discusses thrust analysis and CFD simulations, while experimental results are presented for a prototype USCV in Section VI. Conclusions and future research directions are discussed in Section VII.

II. CONTROL PRINCIPLES

Figure 1 presents a schematic illustrating the design of a USCV employing the proposed pump-valve propulsion system, which includes a twin hull composed of left (L) and right (R) sides, which are denoted herein as sides A and B, respectively, with submerged pumps (6A and 6B), water flow inlets (8A and 8B), rear and fore outlets (1A, 1B, 4A, 4B,

7A, and 7B), and rear and fore magnetic valves (2A, 2B, 3A, 3B, 5A, and 5B) positioned in mirror symmetry on the A and B sides. Each side includes three magnetic valves, where one (5A or 5B) is normally opened and the other two (2A, 3A or 2B, 3B) are normally closed. Here, the pump-valve propulsion force is manipulated by controlling the thrust and direction of the water flows derived from the two submerged pumps according to control data provided by microprocessors. Accordingly, USCV motion control is achieved by guiding the direction of the water flow through each section of the water conduits by controlling the submerged pumps and by the opening and closing the magnetic valves.

The operational principles of the control system are illustrated by the flow chart given in Figure 2. We note that the initial boot-up of the system turns on submerged pumps 6A and 6B, such that the vessel will move forward by default. All magnetic valves are disabled by default when the system boots up. At this moment, water flow can only proceed through the middle front outlets 7A and 7B because 5A and 5B are normally open. In fact, turning on valves 2A and 2B, and 5A and 5B can also move the vessel forward, because water can flow only through rear outlets 1A and 1B. The flow chart also illustrates how left and right turns, and backward motion are conducted.

III. SYSTEM HARDWARE DESIGN

As illustrated in Figure 3, the system is composed of an STM32 master board, a buck converter, a mode indicator, a pump driver, an R12DS wireless receiver, an AT10 remote controller, light sensors, power modules, magnetic valve drive modules, and electronic speed controllers (ESCs). In addition, an image of the actual assembled control system is given in Figure 4, and a hardware connection diagram is presented in Figure 5, which shows the connections from the controller to the drivers and actuators.

The STM32 microprocessor is efficient and inexpensive, and provides a variety of general-purpose input/output (GPIO), serial peripheral interface (SPI), USART, and flexible library functions. The controller program was written and debugged using Keil μ Vision software. The STM32 microprocessor executes instructions according to the electrical signals obtained from light sensors or ESCs in accordance with transistor-transistor logic (TTL) [29].

The power module was constructed from three Li-ion batteries [30] with output voltages of 7.4, 12, and 48 V owing to the various voltage requirements of the hybrid system. For example, the rated input voltage of the R12DS wireless receiver ranges from 4.6 to 10 V, where 7.4 V was applied herein, but those of the magnetic valves and submerged pumps are 12 V and 48 V, respectively. Meanwhile, the STM32 master board operates at 5 V. Therefore, the 12 V Li-ion battery was also connected to a buck converter, which outputs an adjusted voltage of 4.8 V for the STM32 master board.

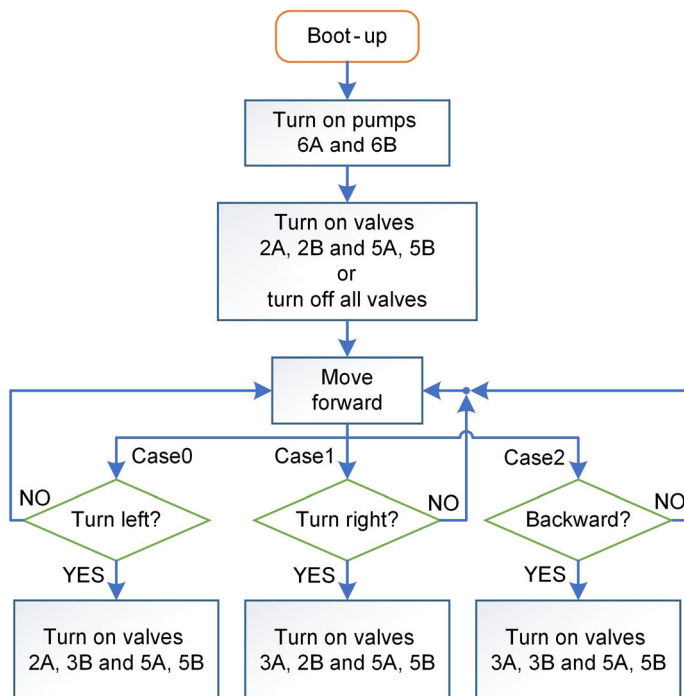The mode indicator consists of three light-emitting diodes (LEDs) that are activated according to the mode flag in the

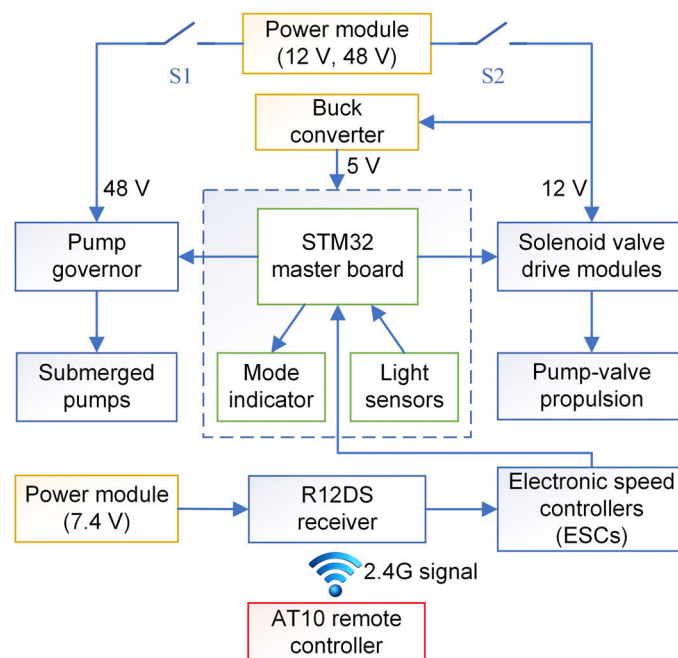**FIGURE 2.** Operational principles of pump-valve propulsion.

FIGURE 3. Schematic illustrating the control system architecture.

controller program [31], [32]. In addition, three light diffuse reflection sensors are respectively affixed to the middle-front, left, and right sides of the twin hull, and are used for obstacle detection. We note that these light sensors are not employed for distinguishing target floating objects requiring collection from actual obstacles, and can only detect obstacles lying

above the water surface, such as large pieces of driftwood, seawalls, piers, and docks. These sensors have a rated input voltage of 5 V and detection ranges of 0 to 80 cm. Each light sensor has three wires, consisting of a positive, negative, and feedback-signal wire, the last of which outputs a low voltage signal when the light sensor detects an obstacle. Three
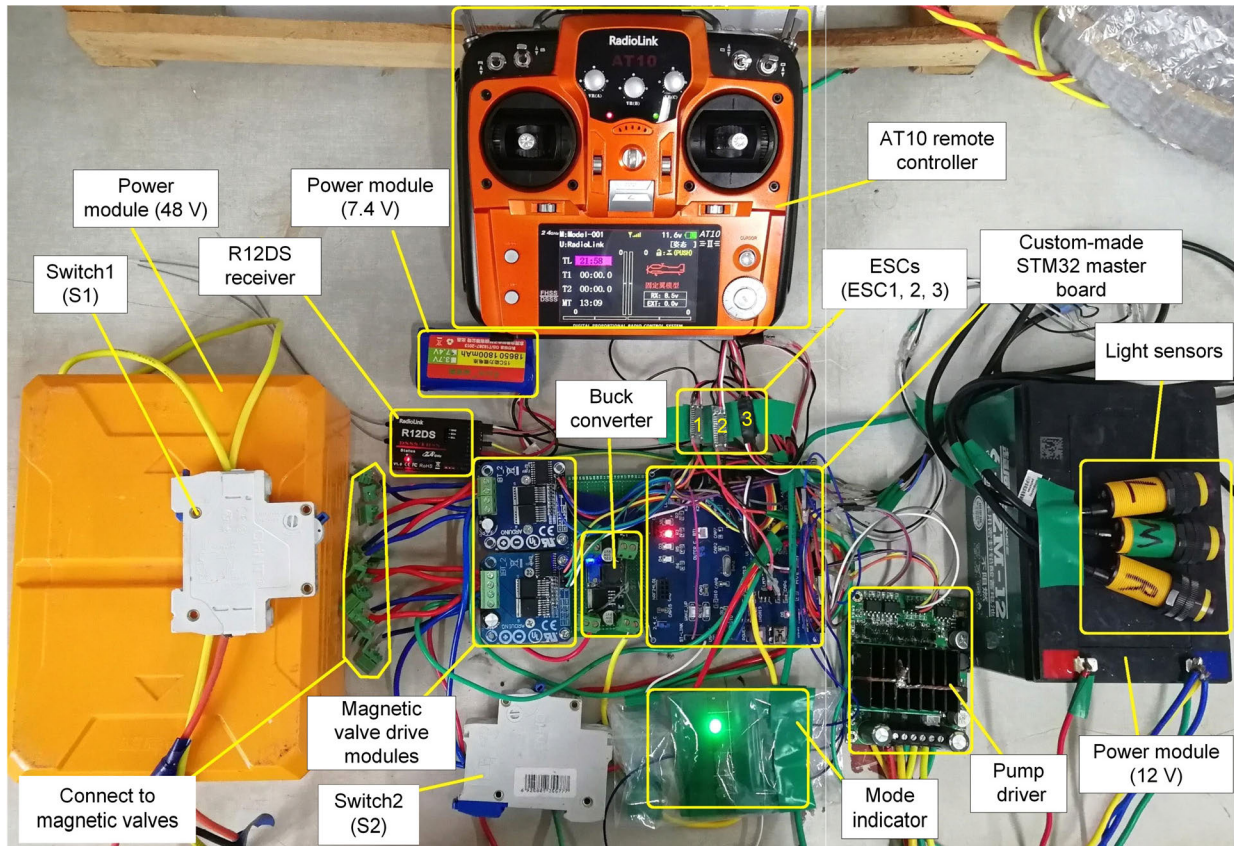
FIGURE 4. Image of the actual hardware control system operating in mode 1.

bidirectional brush ESCs receive the pulse-width modulation (PWM) signals from the R12DS wireless receiver, which included wireless matching to the 2.4 GHz signal of the AT10 remote controller. The designed functions in the program, such as mode-switching and vessel motion control, are then realized based on the electrical level fluctuations from the light sensors and ESCs. We note from Figure 4 that the three ESCs, labeled ESC1, ESC2, and ESC3 from left to right, each have two output pins "a" and "b." Hence, the output signals are denoted as ESC1a, ESC1b, ESC2a, ESC2b, ESC3a, and ESC3b.

It should be noted that the magnetic valve drive modules and the submerged pump drivers are direct current (DC) motor drivers [33]. Meanwhile, the maximum power of a single pump motor is rated at 300 W in theory, but it has a rated voltage of 48 V. Therefore, a high-power DC motor driver with an input voltage ranging from 0 to 60 V was designed using International Rectifiers IRLS3036 N-channel metal oxide semiconductors (NMOSs). The maximum rated current of each pump driver was 100 A with an on-resistance of only 0.0015 ohms, which guarantees the operational stability of the pump motor. In contrast, the rated power of a single magnetic valve is only 18 W. Accordingly, a high-power DC motor driver is not necessary, regardless of the cost and power dissipation capabilities. Therefore, two H-bridge

DC motor drivers were designed using Top Electronics BTN7970 NMOSs. The input voltage of each magnetic valve drive module is between 0 and 27 V, and the maximum drive current is 43 A, which is sufficient to drive all six of the magnetic valves shown in Figure 1. The various power modules are clearly shown in Figure 4. We also note from Figure 5 that two magnetic valve drive modules are used to drive the six valves. The input ports of the magnetic valve drive modules are connected to GPIO pins PB8, PB9, PB10, and PB11 of the STM32 microprocessor. The pump driver connects to GPIO pins PB0 and PB1 of the STM32 microprocessor, which can activate the two submerged pumps simultaneously.

IV. OVERALL SYSTEM SOFTWARE STRUCTURE

A. CONTROLLER PROGRAM DESIGN

The pseudocode of the STM32 interface program is given as Algorithm 1, which is described according to the control data format definitions listed in Table 1. Accordingly, we note that the control data format from the AT10 remote controller is defined as $P1P2 + K1K2 + K3K4 + M1M2$, which stores and recognizes the control instructions received. All GPIO pin speeds were set to 50 MHz. Furthermore, an obstacle-detection approach using the light sensors to control the vessel motion was applied.

Algorithm 1 Pseudocode of the USCV Control System (See Definitions in Table 1)

initialize Switch to Mode 1 by default. Set mode flag bit: *mode* = 1

while 1 **do**

If the mode flag bit equals 1 **then**

Switch to manual remote-control mode (mode 1): Turn on *L*1, *D*2, and *BEEP* once.

   while *mode* = 1 **do**

      Await instructions from the AT10 remote controller.

      If mode-switch control bits *M*1 = 1 and *M*2 = 0 or the mode switching key is pressed **then**

         Set *mode* = 2

      end if

   end while

end if

If *mode* = 2 **then**

Switch to self-automated cruise mode (mode 2): Turn on *L*1, *L*2, *D*3, and *BEEP* twice.

   while *mode* = 2 **do**

   Turn on all pumps at 75% of rated power (set $\theta = 75$).

   Await instructions from light sensors.

   Await mode-switching instructions from the AT10 remote controller.

      If *M*1 = 1 and *M*2 = 0 or the mode switching key is pressed **then**

         Set *mode* = 3

      end if

   end while

end if

If *mode* = 3 **then**

Switch to self-locking remote-control mode (mode 3): Turn on *L*1, *L*2, *L*3, *D*4, and *BEEP* three times.

   while *mode* = 3 **do**

   Turn on all pumps at 100% of rated power (set $\theta = 100$).

   Await instructions from the AT10 remote controller.

      If *M*1 = 1 and *M*2 = 0 or the mode switching key is pressed **then**

         Set *mode* = 1

      end if

   end while

  end if

end while

The present work adopts a nonlinear infinite approximate pump power control method that is specialized for controlling the jet force of the pump-valve propulsion system more efficiently. The duty-cycle control law K_p can be expressed as

$$K_p = \frac{\arctan(F_c)}{\pi/2} \times M, \quad (1)$$

$$F_c = (\sqrt{\theta - 24}) \times D, \quad (2)$$

where M is the multiplication factor, F_c is the correction function, θ is the pump power control term representative of

TABLE 1. Control data format definitions.

Character	Definition
θ	Pump power control term
mode	Mode flag bit, ranges from 1 to 3
*P*1 *P*2	Pump control bits connected from PB0 and PB1 to pump drivers
*K*1 *K*2	Turn left/right motion control bits connected from ESC1a and ESC1b to PB4 and PB5
*K*3 *K*4	Forward/backward motion control bits connected from ESC2a and ESC2b to PB6 and PB7
*M*1 *M*2	Mode-switch control bits connected from ESC3a and ESC3b to PA2 and PA3
BEEP	Active buzzer control bit connected to PB15 of the GPIO module
*L*1 *L*2 *L*3	Control bits of LEDs for the mode indicator
*D*2 *D*3 *D*4	On-board control bits of LEDs

the pump power output as a percentage of its rated output, and D is the change rate factor.

The duty-cycle control law given by Eqs. (1) and (2) includes various control variables such as θ that enable the programmer to not only control the pump power in a more straightforward manner, but can also decrease the software development period and facilitate system upgrades (e.g., the pump output power can be easily varied by changing the value of θ). The pump-control waveform obtained from pump driver control pins PB0 and PB1 are shown in Figures 6(a)–(d) with θ values of 25, 50, 75, and 100, respectively. We also plot the relationship between K_p and θ in Figure 7 with different values of D. We can see that the curves gradually approach a maximum value with increasing θ. In addition, K_p can be employed to determine the actual output power of each pump P_{act} as

$$P_{act} = \alpha K_p P_{max} = U_p I_p, \quad (3)$$

where α is the compensation factor for the pump power, which resides in the range from 0 to 1, P_{max} is the maximum output power of the pump, which is 300 W, while P_{act} is ultimately the product of the pump-drive voltage U_p and the pump current I_p.

B. VESSEL OPERATIONAL MODES

1) MANUAL REMOTE-CONTROL MODE

The control system resides by default in mode 1 at boot-up. A control diagram for mode 1 operation is presented in Figure 8. This mode ensures operational safety because the magnetic valves and submerged pumps are all off by default in mode 1. The STM32 microprocessor continuously detects the TTL level fluctuations from the ESCs in real time, which enables the input power of the pump motors and the vessel motion to be controlled according to the tilt angle of the joystick on the AT10 remote controller.

2) SELF-AUTOMATED CRUISE MODE

A control diagram for mode 2 operation is presented in Figure 9. In mode 2, the STM32 microprocessor no longer
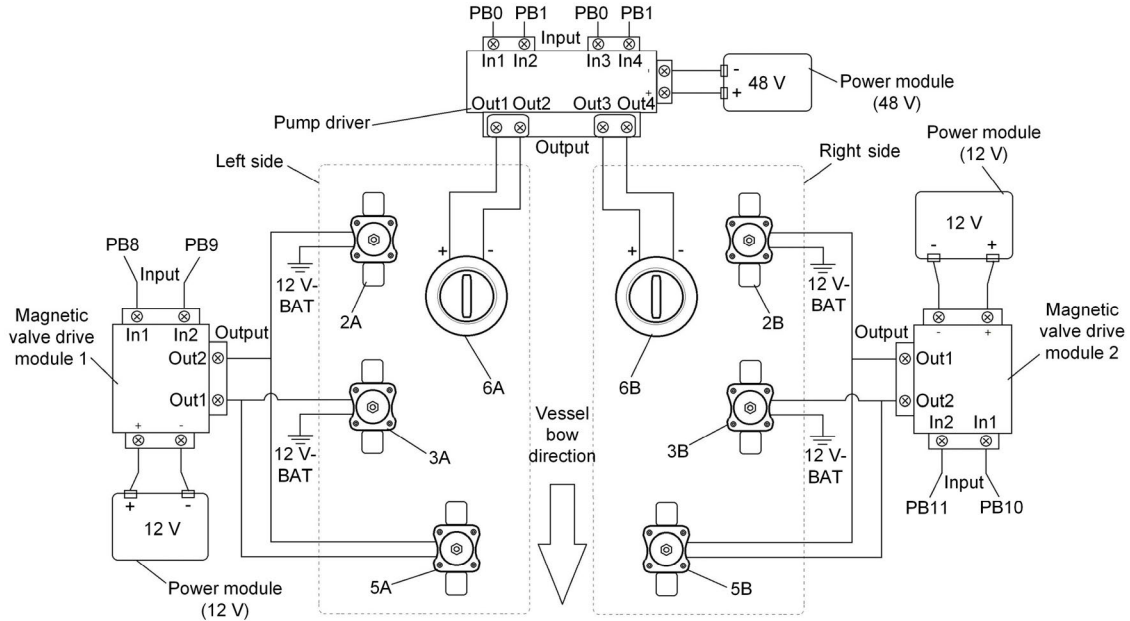
FIGURE 5. Hardware electrical connection diagram of the control system.

accepts motion-control instructions from the ESCs, but rather from the three light sensors affixed to the middle-front, left, and right sides of the twin hull. As such, the corresponding motion-control subprogram is executed according to the feedback signals of the light sensors, as shown in Figure 9. Here, GPIO pins PB0 and PB1 of the STM32 microprocessor are connected to the pump driver, and modulated square wave signals (according to Eqs. (1) and (2) above, and particularly with regard to Figure 6) are input to achieve thrust control [34], [35]. The pump power is set at 75% of the rated power to save energy when no light sensor is triggered. This also represents the cruising speed of the USCV, which about 5 cm/s. However, the pump power will be increased to 100% to avoid collision when obstacles are detected [36]–[38]. For example, an obstacle detected by the middle light sensor will result in a control command making the USCV move backward at the maximum speed of about 12 cm/s.

3) SELF-LOCKING REMOTE-CONTROL MODE

A control diagram for mode 3 operation is presented in Figure 10. In mode 3, the pump power is set at 100% of the rated power at the beginning, resulting in a maximum forward speed of 8 cm/s. This state of forward motion is maintained until the joystick is actuated by the user toward a different direction. For example, to turn the vessel to the left, the user would move the joystick to the left once, whereupon the joystick automatically returns to its neutral position. Meanwhile, the vessel will continue turning left until the joystick is similarly actuated by the user toward a different direction. This is convenient for the operator, and is a distinguishing feature of this operational mode.

V. SYSTEM TESTING

A. THRUST ANALYSIS

A three-dimensional (3D) vessel model was established to evaluate the thrust effect from the pump-valve propulsion system by means of mechanical analysis using a set of mechanical equations that enable the vessel motion to be described with six degrees-of-freedom (DOF) [39]. This is sufficient to predict the motion behavior of an actual USCV, such that the model can be employed for reducing the time and costs of implementing CFD simulations and USCV prototype testing. The model and its coordinate system representing three linear DOF and three rotational DOF are illustrated in Figure 11, which includes surge motion along the X-axis, sway motion along the Y-axis, yaw motion along the Z-axis, roll rotation about the X-axis, pitch rotation about the Y-axis, and heave rotation about the Z-axis.

Specifically, water flow from the pump-valve propulsion system acts only within the X-Y plane. Therefore, we can assume that the vessel is laterally and longitudinally stable, such that the dynamics of roll and pitch can be neglected. The heave dynamics can also be ignored if the vessel is horizontally stable, as would be the case under calm water surface conditions. Therefore, a 3-DOF model can be applied to vessel motion $\partial_{U(3\times3)}$ in the X-Y plane according to a force vector of thrust (X_U, Y_U) and a yaw moment of force N_U, and is defined as

$$\partial_{U(3\times3)} = \begin{bmatrix} X_U & Y_U & N_U \end{bmatrix}^{\mathrm{T}}. \quad (4)$$

In addition, the dynamics of the USCV under (X_U, Y_U) and N_U can be described according to the Newton-Euler formula
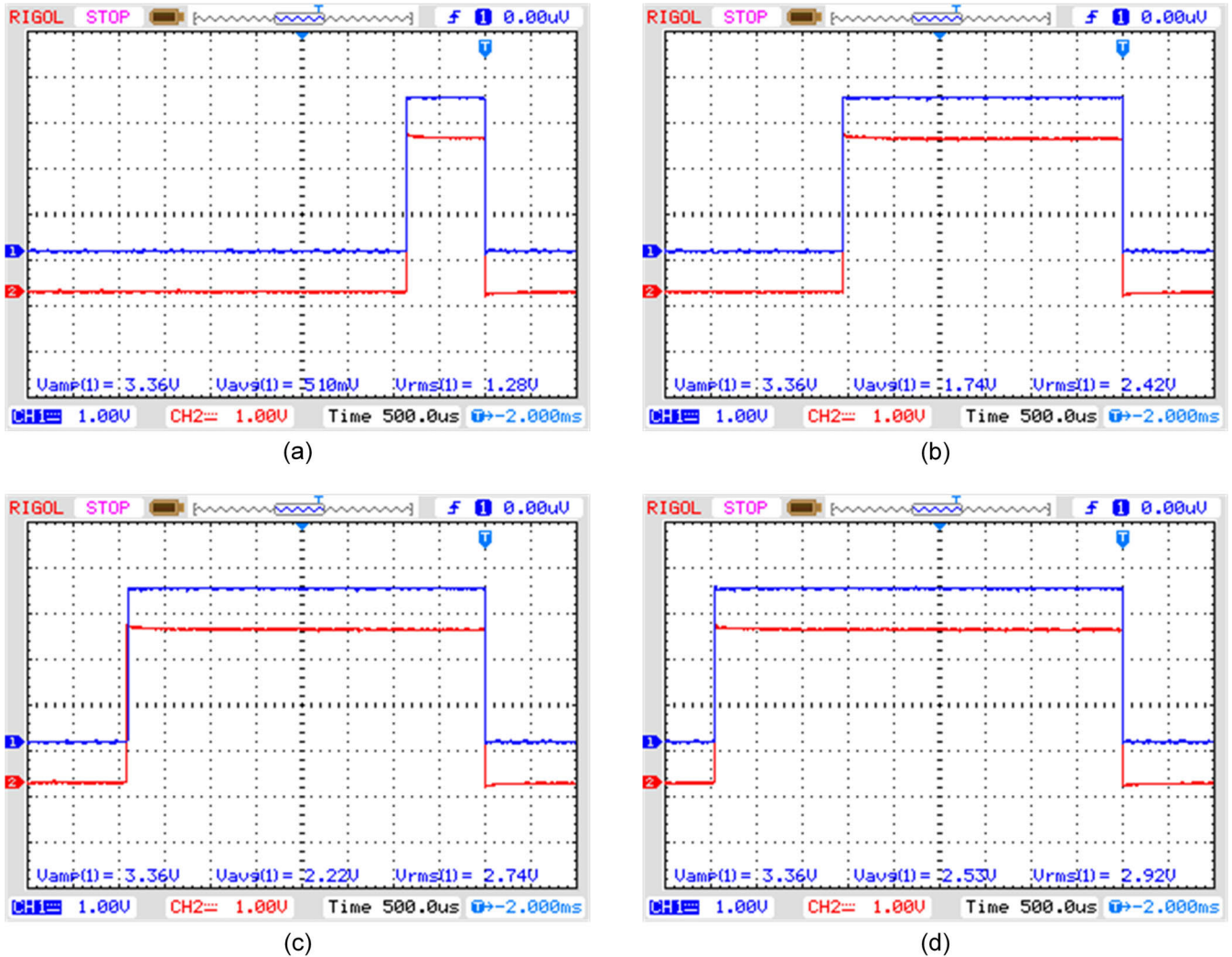
FIGURE 6. Pump-control signal waveforms from pump driver control pins PB0 and PB1 (signals 1 and 2): (a) $\theta = 25$; (b) $\theta = 50$; (c) $\theta = 75$; (d) $\theta = 100$.

as follows [40]–[42].

$$\begin{bmatrix} M_U I_{(3\times3)} & O_{(3\times3)} \\ O_{(3\times3)} & I_Z \end{bmatrix} \begin{bmatrix} \dot{V}_U \\ \dot{\omega}_U \end{bmatrix} + \begin{bmatrix} \omega_U \times M_U V_U \\ \omega_U \times I_Z \omega_U \end{bmatrix} = \partial_U \quad (5)$$

Here, M_U is the total mass of the vessel, $I_{(3\times3)}$ is the 3D unit matrix, I_Z is the rotary inertia, $O_{(3\times3)}$ is the 3D null matrix, ω_U is the angular velocity of the vessel, and V_U is the linear velocity of the vessel.

The thrusts acting on the vessel in the X-Y plane under pump-valve propulsion are illustrated in Figure 12, where F_{1A}, F_{1B}, F_{4A}, F_{4B}, and F_M are the counterthrusts generated from the corresponding fore, rear, and middle front outlets, X_U and Y_U are the respective thrusts from the X-axis and Y-axis directions, where G is the gravity point, and F_U is the resultant thrust on the vessel. Here, F_U is the combined force from outlets 7A and 7B, and can be described by

$$F_U = F_{1A} + F_{1B} + F_M + F_{4A} + F_{4B}. \quad (6)$$

B. MEASUREMENTS AND CFD SIMULATIONS

The thrusts F_{1A}, F_{1B}, F_{4A}, F_{4B}, and F_M established by the above model were measured experimentally under different pump power settings prior to conducting CFD simulations. To this end, we constructed a full-size 3D prototype of the pump-valve propulsion system, which is illustrated in Figure 13. The symmetrical characteristics of the pump-valve propulsion system enabled measurements to be conducted for only the right-side of the pump-valve propulsion system because the thrust values for the right side are equivalent to those for the left side. Accordingly, we measured the water-flow rates through outlets 1B, 4B, and 7B, the flow velocity of inlet 8B, and the flow velocities of outlets 1B, 4B, and 7B on the right side of the system. Then, the corresponding thrusts T_{out} can be calculated according to an increment of momentum within a unit time as

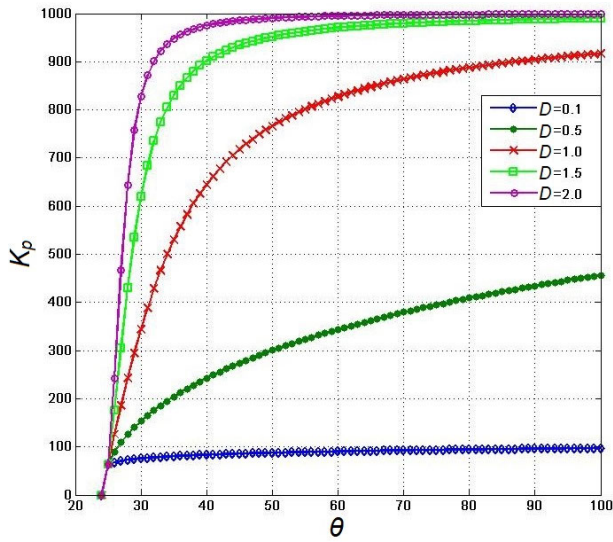$$T_{out} = \varepsilon Q(|V_{in} - V_{out}|), \quad (7)$$

FIGURE 7. Relationship between the duty-cycle control law K_p and control variable θ with different values of the change rate factor D.
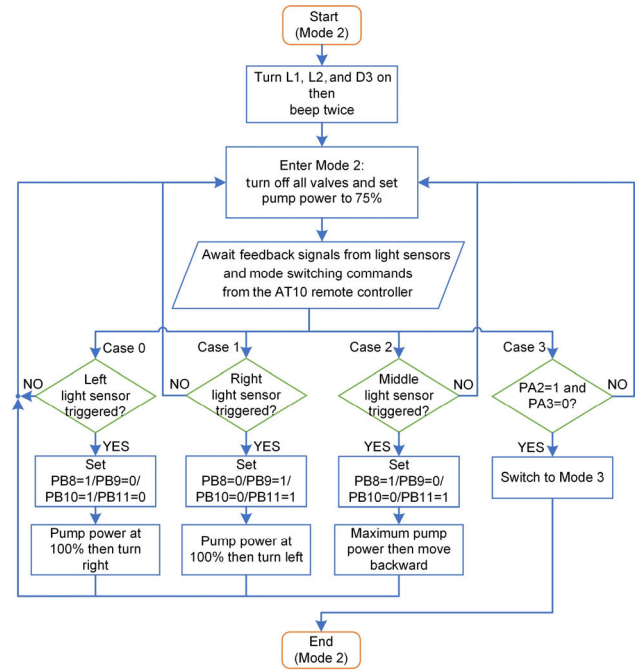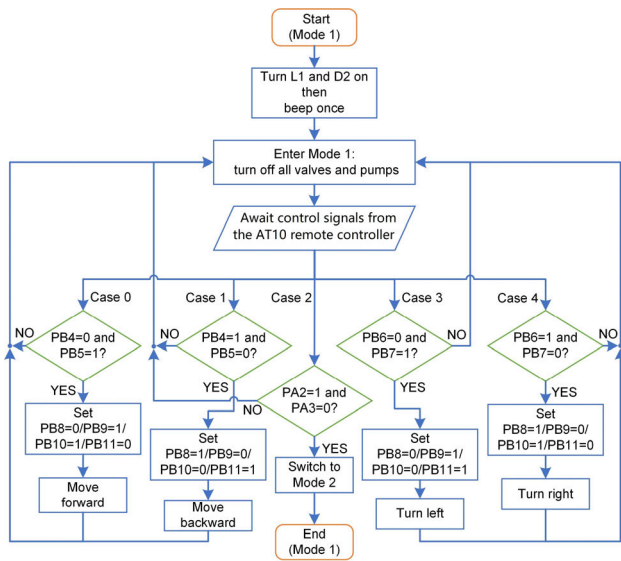

FIGURE 8. Mode 1 control diagram.

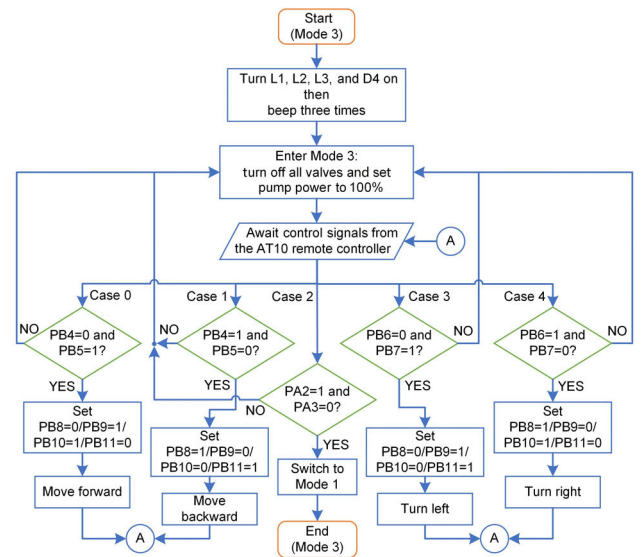**FIGURE 9.** Mode 2 control diagram.

FIGURE 10. Mode 3 control diagram.

where ε is the fluid density, which is set as 1 g/cm^3, Q is the water-flow rate through a given outlet, V_{in} is the flow velocity of inlet 8B, and V_{out} is the flow velocity of a given outlet.

The water-flow rates and flow velocities obtained for the various outlets on the right side of the system under different pump power settings are listed in Table 2. Here, the pump power was controlled using a pump governor that enabled the pump power to be varied from 0% to 100%, where the measurements were obtained at 10% intervals. In addition, an AC-DC clip-on ammeter and a voltmeter were employed respectively to obtain the actual current and voltage values. The data in Table 2 was employed in conjunction with Eq. (7) to determine the thrusts of outlets 1B, 4B, and 7B, which are plotted in Figure 14. We note that the maximum thrusts of

outlets 1B, 4B, and 7B obtained at the highest pump power setting were 14.27 N, 15.28 N, and 12.57 N, respectively, which, as discussed, are equivalent for outlets 1A, 4A, and 7A on the left side. These results were particularly useful for developing a plan for future the optimization of the pump-valve propulsion system.

We then conducted CFD simulations under different USCV motion conditions based on the flow data in Table 2 using Autodesk CFD software. The simulations employed the standard k-epsilon turbulence model, and different flow-trace colors are employed for representing various

TABLE 2. Measured data regarding outlet flow rates and velocities of the model pump-valve propulsion system for various pump power settings.

Pump power (W)	$Q1B$ (L/s)	$Q4B$ (L/s)	$Q7B$ (L/s)	$Q8B$ (L/s)	$V_{out}1B$ (dm/s)	$V_{out}4B$ (dm/s)	$V_{out}7B$ (dm/s)	$V_{in}8B$ (dm/s)
0	0	0	0	0	0	0	0	0
4.19	0	0	0	0.12	0	0	0	0
11.58	0.20	0.19	0.22	0.30	6.4	6.2	7.1	9.6
22.01	0.29	0.26	0.31	0.48	9.1	8.4	9.8	15.1
37.45	0.41	0.33	0.39	0.62	12.9	10.4	12.5	19.8
61.29	0.48	0.40	0.51	0.76	15.3	12.8	16.9	24.1
88.94	0.57	0.46	0.61	0.88	18.2	14.6	19.4	28.0
118.73	0.66	0.52	0.73	1.02	21.0	16.7	23.3	32.5
141.47	0.74	0.59	0.82	1.16	23.5	18.7	26.1	36.8
172.83	0.80	0.68	0.91	1.28	25.5	21.8	28.8	40.8
211.26	0.87	0.76	0.99	1.39	27.8	24.1	31.5	44.2
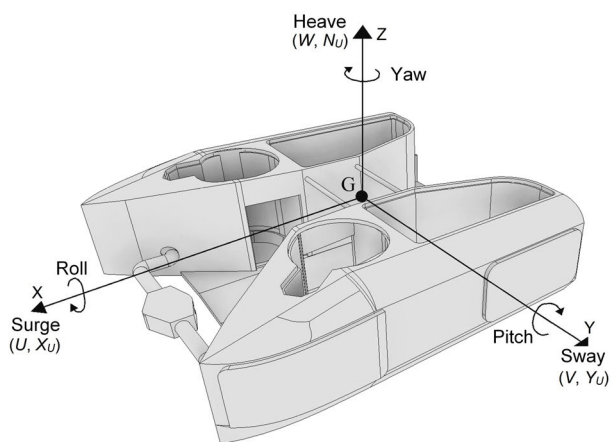
FIGURE 11. USCV model coordinate system definition with all six degrees of freedom (DOF).
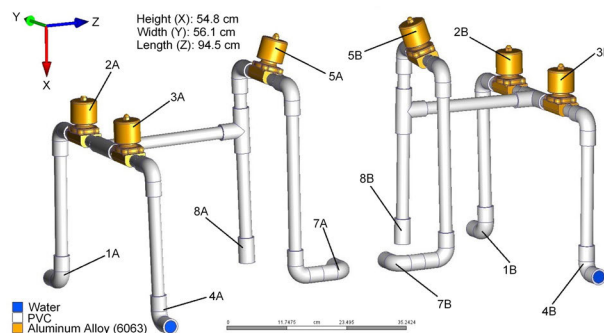

FIGURE 12. Thrusts acting on the USCV in the X-Y plane from the propulsion system (top-view).

FIGURE 13. Illustration of the full-size prototype of the pump-valve propulsion system.

FIGURE 14. Measured thrusts of outlets 1B, 4B, and 7B of the prototype pump-valve propulsion system under different pump power settings.

water-flow velocity magnitudes. However, it is well known that water is an incompressible fluid, such that the outlet fluid velocity must be equal to the inlet fluid velocity under
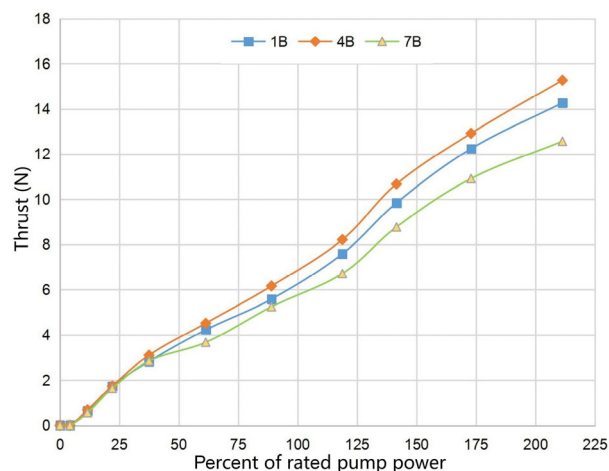
equivalent conditions, such as with identical bore sizes and pump power. The simulation results and settings for the different motion conditions are described as follows.

1) FORWARD MOTION
As shown in Figure 15, the fluid is emitted from the middle front outlets 7A and 7B when it enters from inlets 8A and 8B.
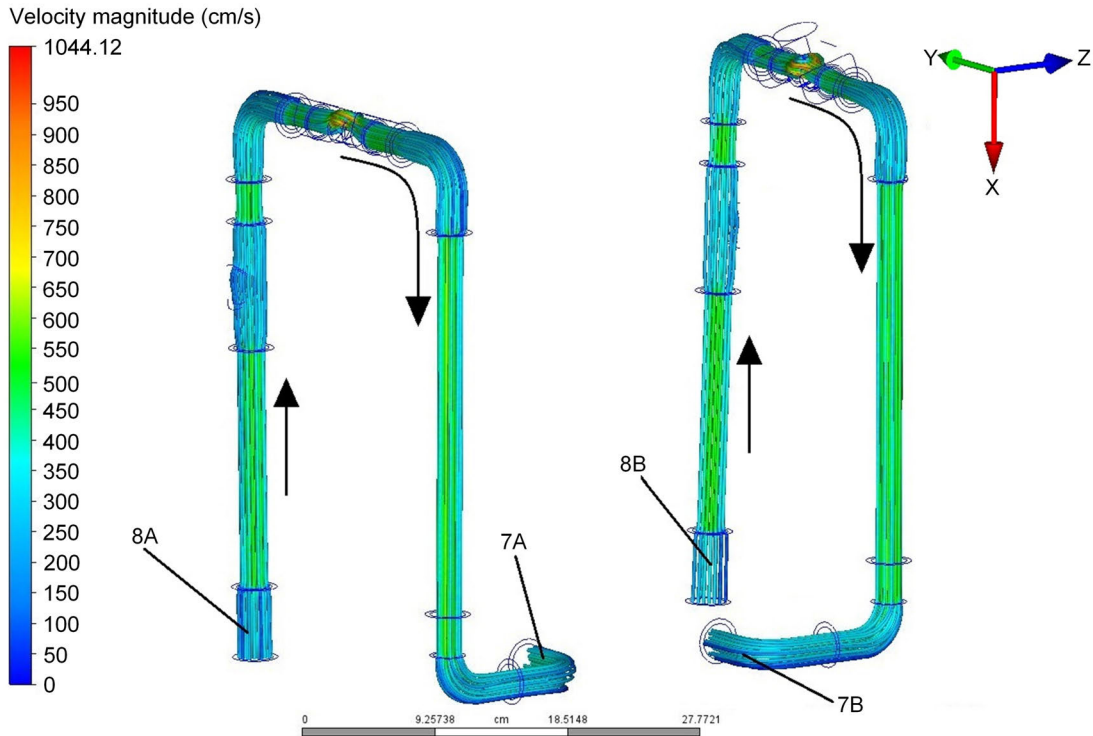
FIGURE 15. Flow traces under forward USCV motion.

Here, none of the valves are activated because valves 5A and 5B are normally open, so the fluid passes directly through them. The boundary conditions are set as follows. The fluid inflow velocities of inlets 8A and 8B are set to 315 cm/s, the static pressures of the open outlets 7A and 7B are set to zero, and the volume flow rates of the closed outlets 1A, 1B, 4A, and 4B are set to zero.

2) BACKWARD MOTION
The simulated conduit flows under this condition are shown in Figure 16. Here, valves 3A, 3B, 5A, and 5B are activated. The boundary conditions are set as follows. The fluid inflow velocities of inlets 8A and 8B are set to 241 cm/s, the static pressures of the open outlets 4A and 4B are set to zero, and the volume flow rates of the closed outlets 1A, 1B, 7A, and 7B are set to zero.

3) TURNING LEFT
The simulated conduit flows under this condition are shown in Figure 17. Here, fluid flows from inlets 8A and 8B, and valves 2A, 3B, 5A, and 5B are activated. Therefore, the boundary conditions are set as follows. The fluid inflow velocities of inlets 8A and 8B are set to 278 cm/s and 241 cm/s, respectively, the static pressures of the open outlets 1A and 4B are set to zero, and the volume flow rates of the closed outlets 1B, 4A, 7A, and 7B are set to zero.

4) TURNING RIGHT
The simulated conduit flows under this condition are shown in Figure 18. The behavior in this case is the opposite of

the left turn motion. Here, the right turn operational state is effected by activating valves 2B, 3A, 5A, and 5B, such that the fluid can flow only through outlets 1B and 4A. Therefore, the boundary conditions are set as follows. The fluid inflow velocities of inlets 8A and 8B are set to 241 cm/s and 278 cm/s, respectively, the static pressures of the open outlets 1B and 4A are set to zero, and the volume flow rates of the closed outlets 1A, 4B, 7A, and 7B are set to zero.

C. ANALYSIS OF CFD SIMULATION RESULTS
The CFD simulation results shown in Figures 15–18 indicate that the flow velocities are greatest when passing through the valves owing to their restrictive cross-sectional areas. Hence, this is the primary cause of turbulent kinetic energy (TKE) losses. In addition, the flow velocity of each inlet and corresponding outlet is equivalent because water is an incompressible fluid. Moreover, the flow traces show that the velocity of water flow increases as the cross-sectional area of a flow channel decreases. Accordingly, the thrust loss T_{loss} from an inlet to an outlet can be described by

$$T_{loss} = |T_{in} - T_{out}|, \tag{8}$$

where T_{in} is the inlet thrust, given as

$$T_{in} = \varepsilon Q V_{in}. \tag{9}$$

In addition, the thrust efficiency η_T can be defined as

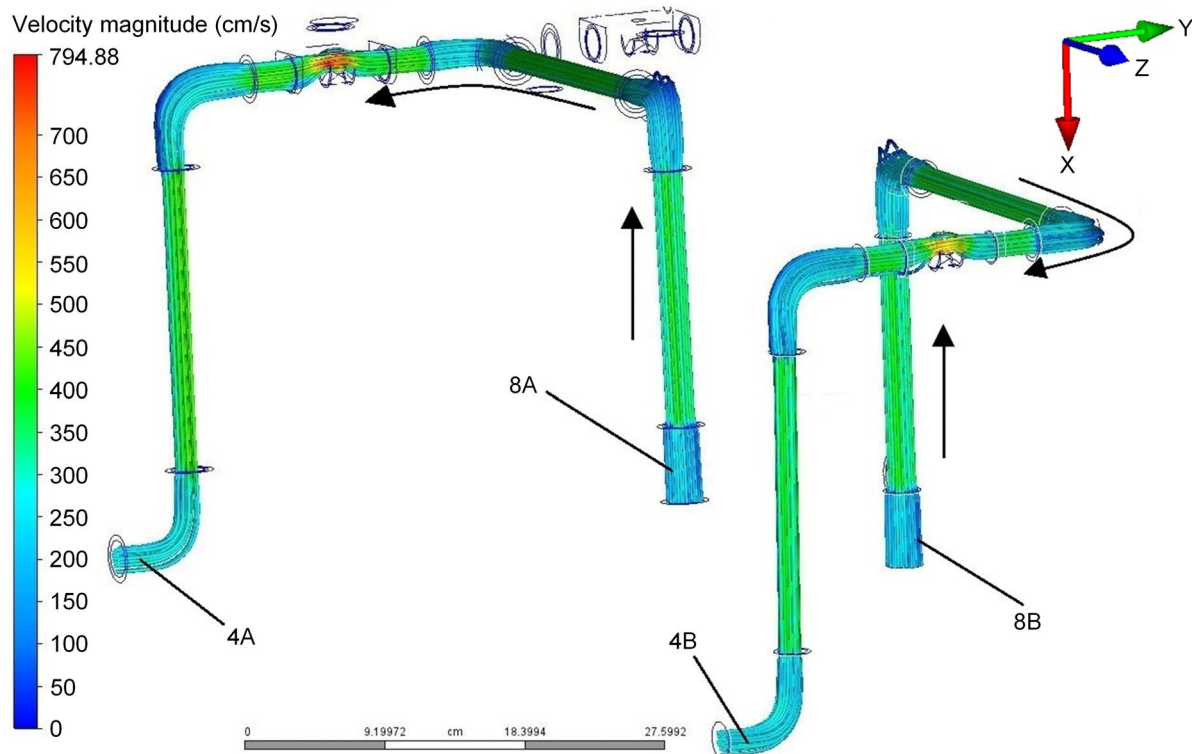$$\eta_T = \frac{T_{in} - T_{loss}}{T_{in}} \times 100\%. \tag{10}$$

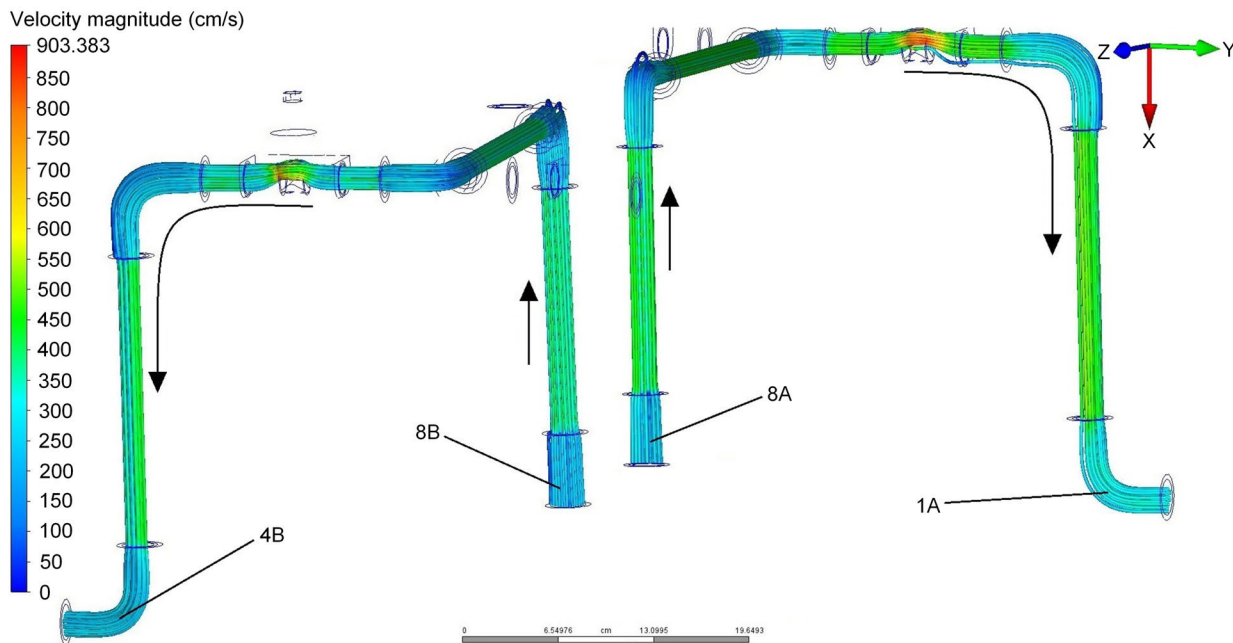**FIGURE 16.** Flow traces under backward USCV motion.

FIGURE 17. Flow traces when the USCV turns left.

The thrust efficiency is a vital parameter for conducting pump-valve propulsion optimization. Then, Eqs. (8) and (9) can be employed respectively to calculate the thrust losses of outputs 1B, 4B, and 7B and the inlet thrusts of 8B for the right-side of the pump-valve propulsion system under different pump power settings based on the data listed in Table 2. In addition, the thrust efficiencies of outlets 1B, 4B, and 7B can be obtained under different pump power settings
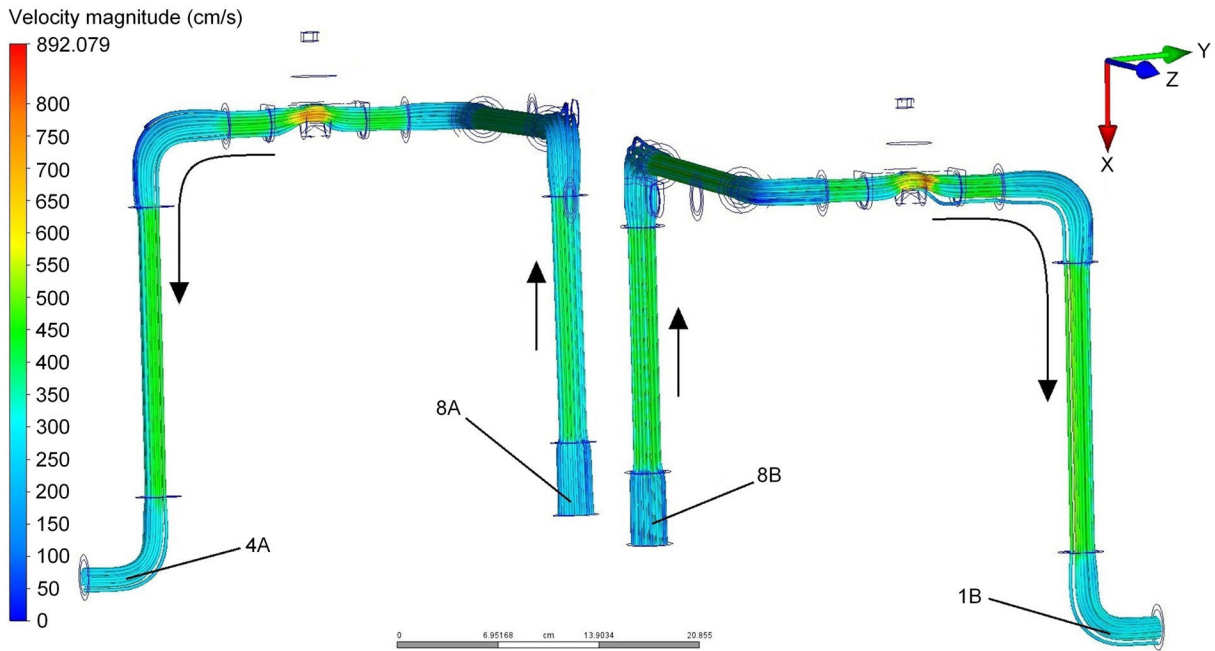
FIGURE 18. Flow traces when the USCV turns right.

TABLE 3. Output thrust losses, inlet thrusts, and thrust efficiencies under different pump power settings.

Pump power (W)	T_{loss} 1B (N)	T_{loss} 4B (N)	T_{loss} 7B (N)	T_{in} 8B (N)	η_T 1B	η_T 4B	η_T 7B
0	0	0	0	0	–	–	–
4.19	0	0	0	0	–	–	–
11.58	2.24	2.2	2.33	2.88	22.2%	23.6%	19.1%
22.01	5.51	5.51	5.61	7.25	24.0%	24.0%	22.7%
37.45	9.45	9.17	9.43	12.28	23.0%	25.3%	23.2%
61.29	14.10	13.80	14.64	18.31	23.1%	24.7%	20.1%
88.94	19.10	18.48	19.39	24.64	22.7%	25.0%	21.3%
118.73	25.56	24.93	26.43	33.15	22.9%	24.8%	20.3%
141.47	32.85	32.00	33.91	42.69	23.1%	25.0%	20.6%
172.83	39.98	39.30	41.30	52.22	23.4%	24.7%	20.9%
211.26	47.17	46.16	48.87	61.44	23.2%	24.9%	20.5%

using Eq. (10). The results of these calculations are listed in Table 3.

The results in Table 3 indicate that the maximum thrust losses of outlets 1B, 4B, and 7B are quite large, and obtain values of 47.17 N, 46.16 N, and 48.87 N, respectively, at the maximum pump power setting. Again, as discussed, these values are equivalent for outputs 1A, 4A, and 7A on the left side. Accordingly, the total thrust loss for the overall USCV is obtained by multiplying the losses based on the right-side data by a factor of 2. As for conventional propellers, the peak efficiencies of water jet propulsion systems are commonly 60% or more [43]. However, the thrust efficiency of the proposed pump-valve propulsion system is approximately 25% at most. This can be attributed to two main reasons. First, the pump-valve propulsion system employs too many conduits, which restricts the movement of water. Second,

commercial water jet propulsion systems have been subject to design optimization, which has a pronounced effect on the thrust efficiency. Accordingly, low thrust efficiency is the major shortcoming of the proposed pump-valve propulsion system, and future work will focus on optimizing the design.

VI. REAL-WORLD TESTING

A simple prototype USCV based on the pump-valve propulsion system was fabricated to validate the CFD simulation results and demonstrate the functionality of the control system. Then, motion experiments were conducted on the surface of an artificial lake under calm conditions. Accordingly, the tests consisted of observing the operational effects and testing the control functions. The maneuvering experiments consisted of forward motion, right turning, left turning, and backward motion states.
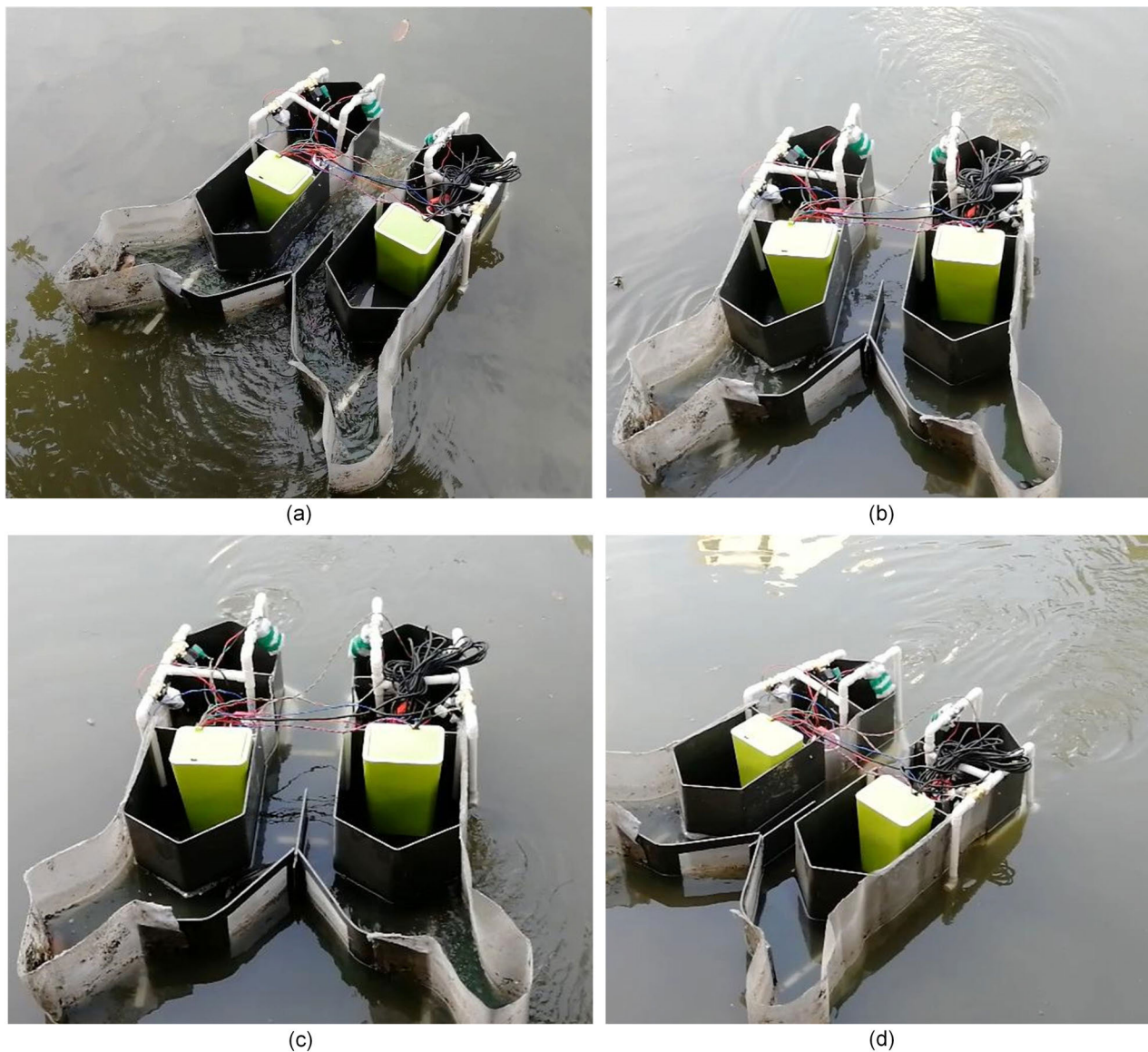
FIGURE 19. Prototype USCV operation under different motion states: (a) forward motion; (b) turning right; (c) turning left; (d) backward motion.

TABLE 4. Measured parameters of the prototype USCV.

Parameter	Value	Unit
Maximum backward speed	12	cm/s
Maximum forward speed	8	cm/s
Maximum single pump power	300	W
Maximum forward thrust	25	N
Maximum backward thrust	28.5	N
Maximum turning rate	5	deg/s
Maximum control distance	4	km
Cruise duration	1.5–4	hour
Total mass	50	kg
Total cost	2968	yuan
Twin-hull size	1330 (length) × 950 (width) × 330 (height)	mm
Conduit bore size	25	mm
Supply voltages	5, 7.4, 12, 48	V
Communication frequency	2.4–2.525	GHz

The relevant data from the vessel maneuvering experiments are listed in Table 4. In addition, we captured images during forward motion, right turning, left turning, and backward motion maneuvers, as shown in Figures 19(a)–(d). The control system was observed to function normally for all maneuvers and the underwater disturbances pertaining to water jet action in each motion state were observed to coincide with the results of CFD simulation. Nonetheless, our present design is susceptible to three main limitations. First, the mode switching logic indicates that the controller cannot go from mode 3 to mode 2 or mode 1, but only from mode 1 to mode 2, and mode 3. Second, three independent batteries must be charged, which is inconvenient for system maintenance. Third, system control relies on the AT10 remote controller, and, hence, the system lacks compatibility. However, we can expect that the development of artificial intelligence using cellular network techniques will make online control feasible in the near future.

We should emphasize that a significant proportion of the thrust generated by the pump-valve propulsion system was expended on surface object collection, and, as discussed, the prototype USCV has not been subjected to optimization. Therefore, the cruising speed of the USCV was generally less than that of conventional propeller watercraft, which typically have a design speed greater than 1 m/s [44]–[46]. This can be mitigated to some extent by equipping the USCV with conventional propellers for use in clear water areas without floating debris and vulnerable wildlife.

VII. CONCLUSION AND FUTURE DIRECTIONS

This study presented a specialized control system for USCVs employing a novel pump-valve propulsion system. Vessel control was conducted according to three operational modes, including manual remote-control mode, self-automated cruise mode, and self-locking remote-control mode. The control functionality and algorithm were presented in detail for each operational mode. The use of the arctangent function for the duty-cycle control of the pump provided a nonlinear infinite approximate control method that simplified the implementation of pump power control. The operative thrusts affecting USCV motion control were established based on a 3D vessel model, which formed the basis for defining the motion behavior of a real-world USCV. The effect of the pump-valve propulsion system on USCV motion was established based on CFD simulations and thrust analysis conducted under different motion states, including forward motion, backward motion, left turning, and right turning states. The combined control and pump-valve propulsion system was further demonstrated by its implementation in a prototype USCV. The experiments verified that the combined control and pump-valve propulsion system is a stable, low-cost, and easy-to-use platform that can be upgraded and expanded. These results revealed the limitations of the presently developed control system. In future work, we intend to add new functionality to the control system. This includes adding a data transfer unit (DTU) based on 4G cellular network communication to acquire additional information, such as global position coordinates and battery life, to facilitate the implementation of more complex multi-USCV collection missions.

APPENDIX
USCV CONTROL SYSTEM CODE

The following is a major segment of the STM32 interface program.

```
int main(void)
{
    unsigned char mode = 1; //Switch to Mode 1 by default
    Hardware_Init();    //Hardware initialization
    while(1)            //Main loop
    {
/* * * * * * * * * * * * * * * * * * * * * * * * * * * *
* * * * * * * * * * * * * * * * * * */
    if(mode == 1) //Mode 1: manual remote-control
    mode
    {
        LED_ON(L1);           //Turn on L1
        D2_ON();              //Turn on D2
        for(t = 0; t<2; t++)   //Beep once
        {
            BEEP = !BEEP;
            Delay_ms(80);
        }
        while(mode == 1)
        {
    AT10_Mode1(); //Await instructions from the AT10
    remote controller
            if((M1 == 1&&M2 == 0) || PAin(0) == 1)
            //Switch to mode 2
        {
            mode = 2;
            pump_stop();     //Turn off all pumps
            valve_off();     //Disable all valves
            light_off();     //All lights off
             break;
        }
        }
    }
/* * * * * * * * * * * * * * * * * * * * * * * * * * * *
* * * * * * * * * * * * * * * * * * */
    if(mode == 2) //Mode 2: self-automated cruise mode
    {
        LED_ON(L1);     //Turn on L1 and L2
        LED_ON(L2);
        D3_ON();        //Turn on D3
        for(t = 0; t < 4; t++)    //Beep twice
        {
            BEEP = !BEEP;
            Delay_ms(80);
        }
        while(mode == 2)
```

```
    {
        pump_on(75); //Turn on all pumps (75% power)
        sensor_instruction(); //Await instructions from
        light sensors
    if((M1 == 1&&M2 == 0) || PAin(0) == 1) //Switch
    to mode 3
        {
            mode = 3;
            pump_stop(); //Turn off all pumps
            valve_off();  //Disable all valves
            light_off(); // All lights off
            break;
        }
    }
}
/* * * * * * * * * * * * * * * * * * * * * * * * * * *
* * * * * * * * * * * * * * * * * * * * * * * * */
    if(mode ==3 ) //Mode 3: self-locking remote-control
mode
    {
    LED_ON(L1);        //Turn on L1, L2, and L3
    LED_ON(L2);
    LED_ON(L3);
    D4_ON;                //Turn on D4
    for(t = 0; t < 4; t++)      //Beep three times
        {
        BEEP = !BEEP;
        Delay_ms(80);
        }
    while(mode == 3)
        {
    AT10_Mode3(); //Await instructions from the AT10 remote
            controller
            pump_on(100);  //Turn on pumps
            (maximum power)
            if((M1 == 1&& M2 == 0) || PAin(0) == 1)
            //Switch to mode 1
            {
            mode = 1;
            pump_stop(); //Turn off all pumps
            valve_off(); //Disable all valves
            light_off(); //All lights off
            break;
            }
        }
    }
}
}
```

ACKNOWLEDGMENT

REFERENCES

[1] Z. Yuyi, Z. Yu, L. Huanxin, L. Yunjia, and L. Liang, "Control system design for a surface cleaning robot," *Int. J. Adv. Robotic Syst.*, vol. 10, no. 5, p. 220, Jan. 2013.

[2] X.-F. Yang and L.-G. Chen, "Design and research of amphibious cleaning robot," *DEStech Trans. Environ., Energy Earth Sci.*, pp. 112–116, Jul. 2017, doi: 10.12783/dteees/eesd2017/11986.

[3] T. Yang, Y. Guo, Y. Zhou, and S. Wei, "Joint communication and control for small underactuated USV based on mobile computing technology," *IEEE Access*, vol. 7, pp. 160610–160622, 2019.

[4] W. Xie, B. Ma, T. Fernando, and H. H.-C. Iu, "A new formation control of multiple underactuated surface vessels," *Int. J. Control*, vol. 91, no. 5, pp. 1011–1022, Apr. 2017.

[5] Z. Jiujun, G. Xin, Y. Zhanmin, W. Xiaoyong, and S. Haichao, "Design and implementation of the control system of a flat surface cleaning robot," *The Open Autom. Control Syst. J.*, vol. 7, no. 1, pp. 1971–1978, Oct. 2015.

[6] K. Rudzki and W. Tarelko, "A decision-making system supporting selection of commanded outputs for a ship's propulsion system with a controllable pitch propeller," *Ocean Eng.*, vol. 126, pp. 254–264, Nov. 2016.

[7] E. Simetti and G. Casalino, "Whole body control of a dual arm underwater vehicle manipulator system," *Annu. Rev. Control*, vol. 40, pp. 191–200, Sep. 2015.

[8] A. Vrijdag and D. Stapersma, "Extension and application of a linearised ship propulsion system model," *Ocean Eng.*, vol. 143, pp. 50–65, Oct. 2017.

[9] S. Sivčev, J. Coleman, E. Omerdić, G. Dooly, and D. Toal, "Underwater manipulators: A review," *Ocean Eng.*, vol. 163, pp. 431–450, Sep. 2018.

[10] Z. Liu, Y. Zhang, X. Yu, and C. Yuan, "Unmanned surface vehicles: An overview of developments and challenges," *Annu. Rev. Control*, vol. 41, pp. 71–93, May 2016.

[11] Ø. K. Kjerstad and M. Breivik, "Weather optimal positioning control for marine surface vessels," *IFAC Proc. Volumes*, vol. 43, no. 20, pp. 114–119, Sep. 2010.

[12] D. Hermann, R. Galeazzi, J. C. Andersen, and M. Blanke, "Smart sensor based obstacle detection for high-speed unmanned surface vehicle," *IFAC-PapersOnLine*, vol. 48, no. 16, pp. 190–197, 2015.

[13] B. Xin, L. Xiaohui, S. Zhaocun, and Z. Yuquan, "A vectored water jet propulsion method for autonomous underwater vehicles," *Ocean Eng.*, vol. 74, pp. 133–140, Dec. 2013.

[14] Z. Zhang, S. Cao, W. Shi, X. Luo, H. Wang, J. Deng, and Y. Zhu, "High pressure waterjet propulsion with thrust vector control system applied on underwater vehicles," *Ocean Eng.*, vol. 156, pp. 456–467, May 2018.

[15] S. Gu, S. Guo, and L. Zheng, "A highly stable and efficient spherical underwater robot with hybrid propulsion devices," *Auto. Robots*, pp. 1–13, Jan. 2020, doi: 10.1007/s10514-019-09895-8.

[16] Y. Luo, J. Ai, X. Wang, P. Huang, G. Liu, W. Gong, and J. Zheng, "Controlling-strategy design and working-principle demonstration of novel anti-winding marine propulsion," *Int. J. Nav. Archit. Ocean Eng.*, vol. 12, pp. 48–59, Jan. 2020.

[17] I. A. Fernández, M. R. Gómez, J. R. Gómez, and Á. B. Insua, "Review of propulsion systems on LNG carriers," *Renew. Sustain. Energy Rev.*, vol. 67, pp. 1395–1411, Jan. 2017.

[18] F. D. Kanellos, A. Anvari-Moghaddam, and J. M. Guerrero, "A cost-effective and emission-aware power management system for ships with integrated full electric propulsion," *Electric Power Syst. Res.*, vol. 150, pp. 63–75, Sep. 2017.

[19] G. Kuiper, "New developments and propeller design," in *Proc. 9th Int. Conf. Hydrodyn.*, Shanghai, China, Oct. 2010, pp. 7–16.

[20] H. Zhang and W. Kang, "Design of the data acquisition system based on STM32," in *Proc. Proce. Comp. Sci.*, May 2013, pp. 222–228.

[21] M. Małyszko and M. Wielgosz, "Decision support systems in search, rescue and salvage operations at sea," *Sci. J. Mar. Univ. Szczecin.*, vol. 45, no. 117, pp. 191–195, Mar. 2016.

[22] H. Albitar, K. Dandan, A. Ananiev, and I. Kalaykov, "Underwater robotics: Surface cleaning technics, adhesion and locomotion systems," *Int. J. Adv. Robotic Syst.*, vol. 13, no. 1, p. 7, Jan. 2016.

[23] Z. Lv, J. Zhang, J. Jin, Q. Li, and B. Gao, "Energy consumption research of mobile data collection protocol for underwater nodes using an USV," *Sensors*, vol. 18, no. 4, p. 1211, Apr. 2018.

[24] D. Kang and Y.-J. Cha, "Autonomous UAVs for structural health monitoring using deep learning and an ultrasonic beacon system with geotagging: Autonomous UAVs for SHM," *Comput.-Aided Civil Infrastruct. Eng.*, vol. 33, no. 10, pp. 885–902, May 2018.

[25] K. Shi, Y. Chen, Z. He, J. Wang, and Y. Li, "Design of permanent magnet synchronous motor control system for electric vehicle air conditioning compressor based on vector control," *OALib*, vol. 6, no. 1, pp. 1–9, 2019.

[26] G. Picardi, C. Laschi, and M. Calisti, "Model-based open loop control of a multigait legged underwater robot," *Mechatronics*, vol. 55, pp. 162–170, Nov. 2018.

[27] J. Bae, J. Bak, S. Jin, T. Seo, and J. Kim, "Optimal configuration and parametric design of an underwater vehicle manipulator system for a valve task," *Mech. Mach. Theory*, vol. 123, pp. 76–88, May 2018.

[28] W. Song, J. Jiang, S. Zhao, K. Zhu, and Q. Wang, "The design and application of water jet propulsion boat," in *Proc. Int. Conf. Autom. Mech. Control. Comput. Eng. (AMCCE)*, Jinan, China, Oct. 2015, pp. 187–192, doi: 10.2991/amcce-15.2015.34.

[29] C. Ruan, D. Zhao, Y. Sun, J. Hong, S. Ding, and J. Luo, "Design and testing of a control system associated with the automatic feeding boat for farming chinese river crabs," *Comput. Electron. Agricult.*, vol. 150, pp. 14–25, Jul. 2018.

[30] W. Zhu, J. Shi, and S. Abdelwahed, "End-to-end system level modeling and simulation for medium-voltage DC electric ship power systems," *Int. J. Nav. Archit. Ocean Eng.*, vol. 10, no. 1, pp. 37–47, Jan. 2018.

[31] S. Pervez, F. Babar, and N. Abosaq, "Optimal power management & regeneration schema to support green technology in mobile computing," in *Proc. 4th In. Conf. Energy. Environ. Technol. Equip.*, New York, NY, USA, Sep. 2015, pp. 1–9.

[32] M. Ejaz and M. Chen, "Sliding mode control design of a ship steering autopilot with input saturation," *Int. J. Adv. Robotic Syst.*, vol. 14, no. 3, May 2017, Art. no. 172988141770356.

[33] O. Atlam and M. Kolhe, "Performance evaluation of directly photovoltaic powered DC PM (direct current permanent magnet) motor–propeller thrust system," *Energy*, vol. 57, pp. 692–698, Aug. 2013.

[34] M. Blaich, S. Wirtensohn, M. Oswald, O. Hamburger, and J. Reuter, "Design of a twin hull based USV with enhanced maneuverability," in *Proc. 9th IFAC. Conf. Control. Appl. Marine. Syst.*, Osaka, Japan, Sep. 2013, pp. 1–6.

[35] B. M. O. Al-thobaiti, I. I. M. Abosolaiman, M. H. M. Alzahrani, S. H. A. Almalki, and M. S. Soliman, "Design and implementation of a reliable wireless Real-Time home automation system based on Arduino uno single-board microcontroller," *Int. J. Control, Autom. Syst.*, vol. 3, no. 3, pp. 11–15, Jul. 2014.

[36] H. L. Chan and K. T. Woo, "Closed loop speed control of miniature brushless DC motors," *J. Autom. Control. Eng.*, vol. 3, no. 4, pp. 329–335, Aug. 2015.

[37] N. Eric and J. W. Jang, "Study on vehicle accident avoidance system using Kinect depth sensor along with notifications on mobile devices," *Int. J. Appl. Eng. Res.*, vol. 12, no. 20, pp. 9723–9727, Aug. 2017.

[38] X. Liu, Y. Li, J. Zhang, J. Zheng, and C. Yang, "Self-adaptive dynamic obstacle avoidance and path planning for USV under complex maritime environment," *IEEE Access*, vol. 7, pp. 114945–114954, 2019.

[39] J. M. Larrazabal and M. S. Peñas, "Intelligent rudder control of an unmanned surface vessel," *Expert Syst. Appl.*, vol. 55, pp. 106–117, Aug. 2016.

[40] K. A. N. Jørgensen, "State estimation with wave filtering for an unmanned surface vehicle," M.S. thesis, Dept. Eng. Cybern., Norwegian Univ. Sci. Technol., Trondheim, Norway, 2011.

[41] O. N. Lyngstadaas, T. E. Saeterdal, M. E. N. Sorensen, and M. Breivik, "Improvement of ship motion control using a magnitude-rate saturation model," in *Proc. IEEE Conf. Control Technol. Appl. (CCTA)*, Copenhagen, Denmark, Aug. 2018, pp. 75–81.

[42] D. Wang and M. Fu, "Adaptive formation control for waterjet USV with input and output constraints based on bioinspired neurodynamics," *IEEE Access*, vol. 7, pp. 165852–165861, 2019.

[43] V. Durán-Grados, J. Mejías, L. Musina, and J. Moreno-Gutiérrez, "The influence of the waterjet propulsion system on the ships' energy consumption and emissions inventories," *Sci. Total Environ.*, vols. 631–632, pp. 496–509, Aug. 2018.

[44] M. Tadros, M. Ventura, and C. G. Soares, "Optimum design of a container ship's propeller from Wageningen B-series at the minimum BSFC," in *Proc. 18th In. Conf. Marit. Assoc. Mediterr. (IMAM)*, Varna, Bulgaria, Sep. 2019, p. 269.

[45] B. Taskar, K. K. Yum, S. Steen, and E. Pedersen, "The effect of waves on engine-propeller dynamics and propulsion performance of ships," *Ocean Eng.*, vol. 122, pp. 262–277, Aug. 2016.

[46] X. Liu and W. He, "Performance calculation and design of stratospheric propeller," *IEEE Access*, vol. 5, pp. 14358–14368, 2017.
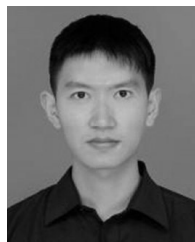
YAOJING LUO received the B.S. degree in electronic information science and technology from the Henan University of Science and Technology, Henan, China, in 2016. He is currently pursuing the Eng.D. degree with the College of Electrical Engineering, Guangxi University, Nanning, China. His current research interests include high voltage, wireless communication, detection technology, and their application to control.

JIAOYAN AI received the M.D. and Ph.D. degrees, in 2000 and 2003, respectively. She has been Professor of electronic science with the College of Electrical Engineering, Guangxi University, Nanning, China, since 2011. Since 2000, she has also been working on intelligent control and automation applied to various fields, such as environment, industry, and agriculture. Her current works focus on two main parts, automatic monitoring of environmental quality and environmental modeling, analysis and visualization.
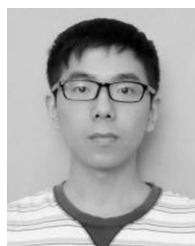
JIANWU ZHENG received the B.S. degree from the University of South China, Hengyang, in 2017. He is currently a Graduate Student with the College of Electrical Engineering, Guangxi University, Nanning, China. His research interests include control theory and intelligent control systems.

JUFENG WANG received the Eng.D. degree in electrical engineering from the Wuhan University of Hydraulic and Electrical Engineering, Hubei, China, in 1999. He is currently a Chief Professor and an Eng.D. Supervisor with the College of Electrical Engineering, Guangxi University, Nanning, China. His research interests include high voltage and modern lightning protection technology.

• • •